

REGULATED STAR FORMATION IN FORMING DISK GALAXIES  
UNDER ULTRAVIOLET RADIATION BACKGROUNDHAJIME SUSA<sup>1</sup>

DEPARTMENT OF PHYSICS, KONAN UNIVERSITY, OKAMOTO, KOBE, JAPAN

<sup>1</sup> SUSA@KONAN.AC.JP*Draft version October 27, 2018*

## ABSTRACT

We perform radiation hydrodynamics simulations on the evolution of galactic gas disks irradiated by ultraviolet radiation background. We find gas disks with  $N_{\text{H}} \gtrsim 10^{21} \text{ cm}^{-2}$  exposed to ultraviolet radiation at a level of  $I_{21} = 1$  can be self-shielded from photoheating, whereas the disk with  $N_{\text{H}} \lesssim 10^{21} \text{ cm}^{-2}$  cannot. We also find that the unshielded disks keep smooth density distribution without any sign of fragmentation, while the self-shielded disks easily fragment into small pieces by self-gravity, possibly followed by star formation. The suppression of star formation in unshielded disks is different from photoevaporation effect, since the assumed dark halo potential is deep enough to keep the photoheated gas. Presence of such critical threshold column density would be one of the reason for the so-called down-sizing feature of present-day galaxies.

*Subject headings:* galaxies: formation — radiative transfer — hydrodynamics

## 1. INTRODUCTION

Recent advances of available computational resources enable us to simulate the entire disk galaxy to investigate parsec scale structures in the disk(Wada & Norman 2007; Robertson & Kravtsov 2007; Tasker & Bryan 2008; Saitoh et al. 2008). In addition, numerical techniques on Radiation HydroDynamics (RHD) simulations are now being developed, especially in the field related to the cosmic reionization(Gnedin & Abel 2001; Mellema et al. 2006; Rijkhorst et al. 2006; Susa 2006; Iliev et al. 2006; Yoshida et al. 2007; Qiu et al. 2007; Whalen & Norman 2008; Altay et al. 2008). Using these schemes, we are now ready to tackle the numerical simulations of the detailed structures in galactic disks coupled with radiation transfer.

The importance of ultraviolet radiation transfer effects on the galaxy formation/star formation in galaxies have been pointed out by several authors. First of all, the observed star formation threshold in galactic disks (Kennicutt 1989; Martin & Kennicutt 2001) could be explained by the self-shielding effects of galactic disks from external ultraviolet radiation field(Schaye 2001, 2004). Schaye (2004) obtained the physical state of the disks exposed to external ultraviolet field, using one dimensional calculation with CLOUDY(Ferland 2000). Based upon the liner stability arguments(Toomre 1964), he has demonstrated that the inner parts of the galactic disks shielded against external radiation field by dust absorption could be gravitationally unstable, whereas the unshielded outer parts of the disks are stable. These results nicely explain the observed features of galactic disks, however, it has not been tested by multi-dimensional RHD simulations.

Secondly, in the context of galaxy formation, radiative feedback by ultraviolet background is expected to be very important especially for low mass galaxies. The photoheating can heat the gas up to  $10^4 \text{ K}$ , which prevent the gas from collapsing, in case the gravitational potential of the dark matter halo is not deep enough

to retain the photoheated gas. Such feedback effects are quoted as photoevaporation, which is well studied at various levels(Umemura & Ikeuchi 1984; Efstathiou 1992; Babul & Rees 1992; Thoul & Weinberg 1996; Barkana & Loeb 1999; Ferrara & Tolstoy 2000; Gnedin 2000; Kitayama et al. 2000, 2001; Susa & Umemura 2004a,b). In addition, there are some evidences in dwarf galaxies that the star formation is suppressed in “hot” ( $\sim 10^4 \text{ K}$ ) phase (Young & Lo 1997a,b), which infer that photoheating can suppress the star formation in galaxies, even if the potential of the dark halo is deep enough to prevent the gas from evaporating. This issue could have a concern to the so-called down-sizing problem in nearby galaxies(Cowie et al. 1996; Kauffmann et al. 2003). They found that old galaxies are massive, while the young ones are less massive. Such trend continues to higher redshift(e.g., Kodama et al. 2004; Erb et al. 2006; Reddy et al. 2006; Papovich et al. 2006). One of the possible interpretation of this feature is that star formation proceed very rapidly in massive galaxies, whereas it is a slow process in less massive galaxies for some reason. Kauffmann et al. (2003) also pointed out that these two groups are well defined, i.e. they have a clear boundary at  $\sim 10^{10} M_{\odot}$  in stellar mass. This critical mass scale is too large to be related to the photoevaporation mechanism, however, photoheating could still be the candidate to explain the down-sizing mass if we can show the mechanism to suppress the star formation even in halos in which the photoionized gas can be inherent.

In this paper, we examine the fragmentation of gas disks embedded in dark halo potential under the ultraviolet radiation field, using the recently developed RHD code RSPH(Susa 2006). This paper is organized as follows. In the next section, the numerical scheme is briefly summarized. In section 3, the setup of numerical simulations are described. We show the results of numerical simulations as well as the analytic estimate in section 4. Sections 5 and 6 are devoted to discussions and conclusion.

## 2. METHODOLOGY

We perform numerical simulations by Radiation-SPH(RSPH) code (Susa 2006). The code can compute the fraction of primordial chemical species  $e^-$ ,  $H^+$ ,  $H$ ,  $H^-$ ,  $H_2$ , and  $H_2^+$  by fully implicit time integration. It also can deal with multiple sources of ionizing radiation, as well as the radiation at Lyman-Werner band.

Hydrodynamics is calculated by Smoothed Particle Hydrodynamics (SPH) method. We use the version of SPH by Umemura (1993) with the modification on the SPH kernel function and symmetrization of equation of motions according to Steinmetz & Müller (1993). We also adopt the particle resizing formalism by Thacker et al. (2000) in which the number of neighbor SPH particles are kept almost constant without sudden changes.

The non-equilibrium chemistry and radiative cooling for primordial gas are calculated by the code developed by Susa & Kitayama (2000), where  $H_2$  cooling and reaction rates are mostly taken from Galli & Palla (1998). As for the photoionization process, we employ so-called on-the-spot approximation (Spitzer 1978). In this paper, we also added the radiative cooling due to metals employing the formula given in Dalgarno & McCray (1972), assuming  $Z = 10^{-2}Z_\odot$ . The metallicity of nearby disk galaxies are normally larger than  $Z = 10^{-2}Z_\odot$ , however, the observed metallicity of the IGM is  $Z \sim 10^{-2}Z_\odot - 10^{-3}Z_\odot$  (e.g., Songaila 2001) which is the ingredient of the galaxies. Since we are interested in the forming disk galaxies, we employ  $Z = 10^{-2}Z_\odot$  in the present set of simulations. Remark that the radiative transitions of heavy elements are not the dominant process of radiative cooling for  $\gtrsim 1000K$  (Boehringer & Hensler 1989; Susa & Umemura 2004a) in case  $Z = 10^{-2}Z_\odot$  is assumed.  $H$  and  $H_2$  molecules are the main coolant of such gas<sup>2</sup>.

The optical depth is integrated utilizing the neighbor lists of SPH particles. In our old scheme (Susa & Umemura 2004a), we create many grid points on the light ray between the radiation source to an SPH particle. In the present scheme, we do not create so many grids. Instead, we create one grid point on the light ray per one SPH particle on its upwind. We find the neighboring 'upstream' particle for each SPH particle on its line of sight to the source, which corresponds to the grid point. Then the optical depth from the source to the SPH particle is obtained by summing up the optical depth at the 'upstream' particle and the differential optical depth between the two particles. The more details are described in Susa (2006). We assess the optical depth for ionizing photons as well as the Lyman-Werner band photons by the method described above. In the present version of the code, the dust opacity is not included in the calculation.

The code is tested for various standard RHD problems(Susa 2006), and already applied to the issues on the radiative feedback effects of first generation stars (Susa & Umemura 2006; Susa 2007). We also take part in the code comparison project with other radiation hydrodynamics codes (Iliev et al. 2006) in which we find reasonable agreements with each other.

## 3. SETUP OF NUMERICAL SIMULATIONS

<sup>2</sup> We have to keep in mind that for low temperature ( $T \lesssim 500K$ ), or high density ( $n_H \gtrsim 10^4\text{cm}^{-3}$ ) realm, even  $Z \sim 10^{-4}Z_\odot$  could be important to decide the fate of cooling gas(Omukai 2000).

We perform numerical simulations of galactic gas disk embedded in a dark halo potential. The dark halo potential is fixed as

$$\Phi_{\text{DH}}(r) \equiv - \left( \frac{27}{4} \right)^{1/2} \left[ \frac{av_1^2}{(r^2 + a_1^2)^{1/2}} + \frac{av_2^2}{(r^2 + a_2^2)^{1/2}} \right], \quad (1)$$

where  $r$  denotes the distance from the center,  $a = 1\text{kpc}$ ,  $a_1 = 0.3\text{kpc}$ ,  $a_2 = 5\text{kpc}$  and  $v_1 = v_2 = 100\text{km/s}$ . Thus the assumed potential is similar to the one employed by Wada & Norman (2007), except that the rotation velocity at given radius is smaller by a factor of 2, since we are interested in the forming galaxies relatively less massive than our Galaxy.

In the present set of simulations, we assume initially uniform disk (Fig. 1) with slight perturbations (displacements of SPH particles are  $\lesssim 10\%$ ). The initial thickness and radius of the disks,  $H_i$ ,  $R_{\text{disk}}$  are  $100\text{pc}$  and  $3\text{kpc}$  for all of the runs, respectively. The initial velocity of the gas particles in the disk are assumed to be the Kepler rotation velocity around the dark halo potential center. Using equation (1), the rotation velocity at the edge of the disk  $r = R_{\text{disk}}$  is as large as  $\sim 100\text{km/s}$ . Thus, the dark halo potential is deep enough to retain the gas even if it is photoheated to  $\sim 10^4\text{K}$ . The initial densities of the disks,  $\rho_i$ , are changed depending on the models, those are listed in Table 2.

The light rays of external ultraviolet radiation field are assumed to be perpendicular to the gas disk. We consider two directions (upward/downward) as shown in Fig. 1. This particular choice of the ray-direction is an approximation if we consider background radiation field exactly, since background photons are coming from all angles. If we take into account such effects, the boundary between the shielded and unshielded regions are softened, which might change the self-shielding effects slightly. However, as far as we keep the number of photons coming into the disk unchanged, the self-shielding condition is also almost unchanged, since it is determined by the balance between the number of recombining hydrogen atoms and the number of photons. The flux of the field at the Lyman limit is given so that the mean intensity at the midplane of the disk equals to  $I_{21} \times 10^{-21}\text{ergs}^{-1}\text{cm}^{-2}\text{Hz}^{-1}\text{str}^{-1}$  in case the opacity of gas disk is ignored. We consider an AGN type spectrum, which is proportional to  $\nu^{-1}$ .

For all of the runs, we employ common physical/numerical parameters of gas disk listed in Table1, while the model dependent parameters are listed in Table 2. As shown in the table, we perform ten runs changing the density of the disk and the intensity of the radiation field.

Since the resolution of the simulation is constrained by the mass of an SPH particle, we have the critical density above which the gravitational fragmentation are not captured properly. According to Bate & Burkert (1997), the density  $n_{\text{H, res}}$  is given as

$$n_{\text{H, res}} = \frac{3}{4\pi m_p} \left( \frac{5k_B T_{\text{min}}}{2Gm_p} \right)^3 \frac{1}{(2m_{\text{sph}} N_{\text{nei}})^2} \quad (2)$$

where  $m_{\text{sph}}$ ,  $N_{\text{nei}}$ ,  $T_{\text{min}}$  denote the mass of each SPH particle, number of neighbor particles and the minimal tem-

perature set in the simulations, respectively. The symbols  $k_B$ ,  $G$ ,  $m_p$  have ordinary meanings, i.e., they represent Boltzmann constant, gravitational constant and proton mass, respectively. In the present set of simulations,  $n_{H,\text{res}}$  equals to  $235 \text{ cm}^{-3}$ , except the runs B/2,Br/2,B/8 and Br/8 in which the mass of a SPH particles is larger than other regular runs by a factor of two or eight (see Table 2). The softening length of gravitational interaction between SPH particles,  $\epsilon$ , is set so as to satisfy

$$\epsilon = \frac{1}{2} \left( \frac{3N_{\text{nei}}m_{\text{SPH}}}{4\pi m_p n_{H,\text{res}}} \right)^{1/3}. \quad (3)$$

This expression guarantees that the self-gravity of a dense clump above  $n_{H,\text{res}}$  is softened.

Given these configurations, we can assess the Toomre's  $Q$  value to understand the stability of the initially uniform disk. Toomre's  $Q$  is defined as

$$Q = \frac{c_s \kappa}{\pi G \Sigma}. \quad (4)$$

Here  $c_s$ ,  $\kappa$  and  $\Sigma$  denote the sound speed of the gas, epicyclic frequency and the surface density of the disk. In case  $Q > 1$  holds, the disk is gravitationally stable because of the Coriolis force/thermal pressure, whereas it is unstable if  $Q < 1$  is satisfied (Toomre 1964).

The actual  $Q$  parameters for three models A, B and C (see Table 2) are plotted in Fig.2. Here  $c_s$  is assumed to be the sound speed corresponding to  $T_{\min} = 300\text{K}$ . Since we assume uniform disks for all models, the disks are more unstable at the outer radii. In the present simulations, the radius of the disks are 3kpc for all models. Thus, there exist critical radii above which the disks are unstable if those are cooled down to  $T_{\min}$ , although the unstable region is narrow for model A (it is unstable only at the edge of the uniform disk). It is worth noting that if we employ  $T_{\min}$  lower than 300K, the unstable region should expand, since the gas temperature will go down to  $T_{\min}$ , that results in smaller  $Q$ .

#### 4. RESULTS

##### 4.1. Stability of the disks without Radiation

First, we present the results for  $I_{21} = 0$ , i.e. no external radiation field. The face-on/edge-on view of the snapshots for the disks in models A, B and C are shown in Fig.3. The snapshots are taken at  $t = 300\text{Myr}$  for model A,  $t = 120\text{Myr}$  for model B and  $t = 40\text{Myr}$  for model C. The particular choices of these times when the snapshots are taken basically corresponds to the time when the time steps at dense gas clumps collapsed below  $n_{H,\text{res}}$  becomes so short ( $\lesssim 10^3\text{yr}$ ) that physical time in numerical computation evolve very slowly. Since the growth time scale of gravitational instability is shorter in denser disks, we take the earlier snapshot in model C than others.

It is clear that the disks in all models fragment into small filaments/knots. At the same time, the inner parts of the disks are stable. As shown in Fig.2,  $Q$  values are larger than unity at smaller radii, whereas they are smaller than unity at larger radii. Therefore, the inner parts of the disks are stable, which is consistent with the present results. In addition, the critical radii outside which the disks are unstable predicted by Toomre criterion are also consistent with numerical results. Indeed, the critical radii

read from Fig.2 are 2.8kpc, 1.6kpc and 0.8kpc for models A,B and C, those are almost consistent with the boundary radii of smooth parts of the disks.

In Fig.4, the phase diagram ( $n_H - T$  plane) of the three runs at the same snapshots as in Fig.3 are shown. The gas temperature in all of the models are cooled efficiently, which are almost close to  $T_{\min} = 300\text{K}$  at high density realm ( $n_H \gtrsim 10^3\text{cm}^{-3}$ ). Such efficient cooling justify the stability argument based upon the  $Q$  values plotted in Fig.2 in which  $T = T_{\min}$  is assumed.

These phase diagram also show that very dense regions above  $n_{H,\text{res}}$  are formed in all of the models. These dense regions correspond to the fragments presented in Fig. 3.

##### 4.2. Effects of Ultraviolet Radiation on the Disk Stability

Now, we show the snapshots of the runs with  $I_{21} = 1$  (Ar, Br and Cr) in Fig.5, i.e.  $t = 300\text{Myr}$  for model Ar,  $t = 120\text{Myr}$  for model Br and  $t = 40\text{Myr}$  for model Cr. The snapshots are synchronized to the corresponding ones in Fig.3. At a first glance we find clear difference from the runs without ultraviolet radiation. In model Cr, we find small filaments and knots as were found in model C, whereas we cannot find any sign of fragmentation in models Ar and Br. In addition, the density of the disks in models Ar and Br becomes lower than that in models A and B. We also observe that the disks are geometrically thicker than the previous ones. In Fig.6, the phase diagrams are shown for models Ar, Br and Cr. In all of the runs, significant amount of materials are photoheated up to  $\gtrsim 10^4\text{K}$  in low density region, that contribute to the disk thickening. Additionally, no very dense gas component above  $n_{H,\text{res}}$  is found in models Ar and Br, while we find it again in model Cr as was found in model C. Thus, these results indicate that the presence of external ultraviolet radiation field suppress the fragmentation of the disks with low density models (Ar and Br), although it does not for high density model (Cr).

##### 4.3. Self-Shielding from Ultraviolet Radiation

The difference between low density models (Ar, Br) and high density model (Cr) comes from the self-shielding effects. Fig.7 shows the density (top), temperature (middle) and HI fraction  $y_{\text{HI}}$  (bottom) distributions along the direction perpendicular to the disks. In model Cr (right column), the gas near the midplane ( $z = 0$ ) is neutral, cold and dense, because of the self-shielding. On the contrary, in models Ar and Br, cold and dense regions near the midplane is relatively smaller than that in model Cr. To be more quantitative, Fig.8 shows the temperature probability distribution functions (PDFs) for models Ar,Br,Cr (top) and A,B,C (bottom). The temperature PDFs show the mass fraction of the disk found within a logarithmic temperature bin  $\Delta(\log T) = 0.06$ . In the runs without radiation field (A,B and C), most of the mass is condensed in the coldest phase at  $T_{\min}$ . On the other hand, the temperature PDFs are broader in the runs with radiation. In models Ar and Br, most of the mass in the disks exist in the hot phase ( $\sim 10^4\text{ K}$ ), while cold phase ( $< 10^3\text{K}$ ) is dominant in model Cr. Such large difference in temperature distribution results in different stability of the disks. According to Fig. 2,  $Q$  values for models Ar and Br satisfy  $\gtrsim 0.5$  if  $r \leq 3\text{kpc}$  and  $T = T_{\min}$ . In actual simulations, we

find  $T \sim 10^4$ K, which means that  $Q$  values are larger by a factor of  $\sqrt{10^4/300} = 5.77$  than 0.5, i.e.  $Q > 1$  is achieved everywhere in the disks for these models. Thus, these disks are stable, while the disk in model Cr is unstable because of its coldness.

A rough estimate of self-shielding criterion for primordial gas has been derived by Susa & Umemura (2000a), who evaluate the shielded photoheating rate to compare with the peak  $H_2$  cooling rate below  $10^4$ K. Remark that heavy elements are not the dominant coolant for  $10^3$ K  $\lesssim T \lesssim 10^4$ K, in case  $Z \lesssim 10^{-2}Z_\odot$  (Susa & Umemura 2004a).

Similar argument is also found in Corbelli et al. (1997), which describes the thermal instability of the primordial gas. According to Susa & Umemura (2000a), the photoheating rate per unit volume at the midplane of the disk for the optically thick limit is given as  $n_{H,c}y_{HI,c}\mathcal{H}$  where <sup>3</sup>

$$\mathcal{H} = \frac{4\pi I_{\nu_L} \nu_L \sigma_{\nu_L}}{3} \frac{\Gamma(\beta)}{1+\beta} \tau_{\nu_L}^{-\beta} \quad (5)$$

Here  $n_{H,c}$  and  $y_{HI,c}$  are the number density of the hydrogen nucleus and HI fraction at the midplane of the disk,  $\sigma_{\nu_L}$  is the photoionization cross section at Lyman limit,  $\nu_L$  is the Lyman limit frequency,  $I_{\nu_L}$  denotes the incident ultraviolet intensity at Lyman limit,  $\Gamma(x)$  is the gamma function.  $\beta$  used in this equation is defined as  $\beta \equiv 1 + (\alpha - 1)/3$ , where  $\alpha$  denotes the spectral index, i.e.,  $I_\nu \propto \nu^{-\alpha}$  is assumed.  $\tau_{\nu_L}$  denotes the optical depth at Lyman limit, which is written as,

$$\tau_{\nu_L} = \frac{\langle y_{HI} \rangle N_H \sigma_{\nu_L}}{2}. \quad (6)$$

Here  $N_H$  denotes the column density of the disk,  $\langle y_{HI} \rangle$  is the HI fraction averaged along the direction perpendicular to the disk. The peak  $H_2$  cooling rate per unit volume below  $10^4$ K is described as  $n_{H,c}^2 \mathcal{C}_{H_2}$ , where  $\mathcal{C}_{H_2} \simeq 10^{-26} \text{erg s}^{-1} \text{cm}^3$  (Shapiro & Kang 1987; Susa & Umemura 2004a). In addition, we assume hydrostatic equilibrium in the vertical direction. As a result, the number density of hydrogen nucleus at the midplane of the disk is related to the column density as follows:

$$n_{H,c} = \frac{\pi G N_H^2 \mu m_p}{2 c_s^2}. \quad (7)$$

Here the gas disk is assumed to be isothermal with sound velocity  $c_s$ . Letting the photoheating rate be equal to the  $H_2$  peak cooling rate, combined with the equations (5), (6) and (7), we obtain the threshold column density  $N_{H,\text{sh}}$ , above which the photoheating is shielded enough for the midplane to cool down to  $\lesssim 1000$ K:

$$N_{H,\text{sh}} = \left( \frac{2^{\beta+3} c_s^2 I_{\nu_L} \nu_L \sigma_{\nu_L}^{1-\beta} \Gamma(\beta)}{3 G \mu m_p \mathcal{C}_{H_2} \langle y_{HI} \rangle^\beta (\beta+1)} \right)^{1/(2+\beta)} \quad (8)$$

Using the present assumptions ( $\alpha = 1$ ,  $I_{21} = 1$ ), we have

$$N_{H,\text{sh}} \simeq 2.5 \times 10^{21} \text{cm}^{-2} \times \left( \frac{I_{21}}{1} \right)^{1/3} \left( \frac{c_s}{10 \text{km s}^{-1}} \right)^{2/3} \left( \frac{\langle y_{HI} \rangle}{0.5} \right)^{-1/3} \quad (9)$$

Here we also assume  $y_{HI,c} = 1$  in the above expression, since it is true for all models Ar, Br and Cr.

<sup>3</sup> The expression  $\mathcal{H}$  is 2 times larger than the equation (A12) in Susa & Umemura (2000a), since the radiation field irradiate the right side of the disk as well as the reverse side in the present simulations.

On the other hand, the initial column density of the disks in models Ar, Br and Cr are  $6.3 \times 10^{20} \text{cm}^{-2}$ ,  $1.3 \times 10^{21} \text{cm}^{-2}$  and  $3.8 \times 10^{21} \text{cm}^{-2}$ , respectively. Thus, the numerical simulations indicate  $1.3 \times 10^{21} \text{cm}^{-2} \lesssim N_{H,\text{sh}} \lesssim 3.8 \times 10^{21} \text{cm}^{-2}$ , which almost agrees with the rough analytic estimate shown above.

#### 4.4. Probability Distribution Functions of Density Field

The differences among the six models (A, Ar, B, Br, C and Cr) are clarified in Fig. 9 in terms of density probability distribution functions (PDFs). Six panels represent the snapshots of the density PDFs for six models. Here the density PDFs are defined as the mass fraction found within a logarithmic density bin  $\Delta(\log n_H) = 0.18$ . The histograms drawn by thin lines represent the initial PDFs, while the thick lines show the evolved ones.

It is clear that in the models A, B, C, and Cr, the PDFs extend beyond the resolution limit  $n_{H,\text{res}}$ . Thus, dense self-gravitating fragments formed in these disks, which would lead to the star formation activities.

It looks strange at first that very dense clumps form beyond  $n_{H,\text{res}}$ , although the gravitational force is softened for  $n_H \gtrsim n_{H,\text{res}}$  (see eq. (3)). In fact, even if gravitational force could be neglected at  $n_H \gtrsim n_{H,\text{res}}$ , matters accrete from the outer envelope. As a result, density (or pressure) of the clump becomes higher than  $n_{H,\text{res}}$ , in order to compensate for the increasing ram/thermal pressure of accreting material.

On the other hand, in the models Ar and Br, PDFs have very sharp cut-off below  $n_{H,\text{res}}$  for the snapshot at  $t = 300 \text{Myr}$  (Ar) and  $t = 120 \text{Myr}$  (Br), although models A and B have clear fragmentation signature at the same snapshots. Thus, the impression from the montage of the disk is correct, i.e. the disk in models Ar and Br do not fragment into dense clouds. This result could be interpreted that the star formation in these disks are heavily suppressed by ultraviolet radiation field.

#### 4.5. Convergence of PDF

The convergence of density PDF is checked for models B and Br. We perform runs with larger SPH particles mass by a factor of two and a factor of eight. These runs are tagged as B/2, Br/2 and B/8, Br/8 (Table 2). Fig. 10 shows the density PDFs for models B, B/2, B/8 (top) and models Br, Br/2, Br/8 (bottom) at  $t = 40, 100, 120 \text{Myr}$ . In the half resolution runs (B/2 and Br/2), the density resolution limits are four times smaller than those in B and Br, because  $n_{H,\text{res}}$  inversely proportional to the square of mass resolution (see equation (2)). Similarly, the density resolution limits in B/8 and Br/8 are 64 times smaller than B and Br. The PDF histograms basically agree very well below  $n_{H,\text{res}}$  as expected.

In the runs B/8 and Br/8, the density resolution limits are so low that the high density regions ( $\gtrsim 100 \text{cm}^{-2}$ ) are not captured properly. As a result, it seems to be difficult to distinguish the PDFs for models B/8 and Br/8 from each other. On the other hand, the results from the runs B/2 and Br/2 indicate the same conclusion as we found in the runs B and Br, since the density resolution is enough to capture the self-shielded dense regions. Thus, the disk

in B/2 fragments due to gravitational instability, whereas that in Br/2 is stable. Therefore we conclude that the resolution of the present regular simulations are enough to capture the fragmentation of the disks under the assumptions we employed, whereas in lower resolution runs such as B/8 and Br/8 are not able to describe the present physical situation.

## 5. DISCUSSION

It should be emphasized that present results directly prove the suppression of star formation activities by ultraviolet background radiation *in halos with  $T_{\text{vir}} > 10^4 \text{ K}$* . It has already been known that the star formation is suppressed in less massive halos with  $T_{\text{vir}} \lesssim 10^4 \text{ K}$ , since the gas in the dark halo potential evaporates due to the high thermal pressure of photoheated gas (Umemura & Ikeuchi 1984; Efstathiou 1992; Babul & Rees 1992; Thoul & Weinberg 1996; Barkana & Loeb 1999; Ferrara & Tolstoy 2000; Gnedin 2000) if the self-shielding effect is not important (Kitayama et al. 2000, 2001; Susa & Umemura 2004a,b). On the other hand, in the present simulations, the gas in the dark halo do not evaporate because of the deep gravitational potential. We find that even in such halos, star formation could be heavily suppressed in case gas is configured to form disks with low column density.

Another important result found in the present calculation is the presence of a clear boundary in the column density of the disk, below which star formation is heavily suppressed. According to the numerical results, the critical column density is  $N_{\text{H}} \sim 1 - 4 \times 10^{21} \text{ cm}^{-2}$ . This threshold is very interesting mainly for two reasons. First, although the present simulations are performed with fixed dark halo mass, we can try to convert the critical column density into dark halo mass. The mass of the uniform disk with given  $N_{\text{H}}$  and disk radius  $R_{\text{disk}}$  is

$$M_{\text{disk}} = 6 \times 10^9 M_{\odot} \left( \frac{R_{\text{disk}}}{10 \text{ kpc}} \right)^2 \left( \frac{N_{\text{H}}}{2.5 \times 10^{21} \text{ cm}^{-2}} \right). \quad (10)$$

Therefore, if the mass of the host dark halo is 7 ( $\simeq \Omega_{\text{B}}/\Omega$ ) times the disk mass, the critical dark halo mass is  $\sim 4 \times 10^{10} M_{\odot}$ . This value is still smaller than the critical scale found by Kauffmann et al. (2003) by a few factor, but if we take into account the internal feedback effects such as UV radiation from internal sources (AGN, massive stars) or supernova, the threshold might account for the observed critical down-sizing mass. We also point out that if we start the simulation from cosmological setup, the threshold mass could be raised more, since photoheating might be able to penetrate deeper into the disk because of initially less dense configurations. Thus, inclusion of such physics as well as starting simulations from cosmological setup are necessary to obtain more precise understanding of star formation in forming disk galaxies.

Secondly, the critical column density is as large as the star formation threshold found in local disk galaxies (Kennicutt 1989; Martin & Kennicutt 2001). In fact, the observed star formation threshold of galactic disks has been investigated by Schaye (2001, 2004) from theoretical side. He suggest that the galactic disk could be gravitationally stable if it is unshielded from the external UV radiation, since  $Q$  value of the photoheated disk easily

exceeds unity. As a result, gravitational fragmentation of the disk is suppressed, so the star formation activities do. Schaye & Dalla Vecchia (2008) performed simple hydrodynamics simulations taking into account the star formation threshold column density using effective equation of state in multiphase medium, although they do not solve radiation transfer equations explicitly. They found the threshold column density is as large as  $4 M_{\odot} \text{ pc}^{-2}$  (Fig.4 and 5 in Schaye & Dalla Vecchia (2008)), which is  $5 \times 10^{20} \text{ cm}^{-2}$  in cgs unit. This value is smaller than that obtained in this paper by a few factor ( $\sim 2.5 \times 10^{21} \text{ cm}^2$ ). The basic mechanism they propose to suppress the star formation of the disk is same as the one found in the present simulations, except that we do not include the effects of dust extinction required especially for present-day disk galaxies. The gas disk is more easily self-shielded by dust absorption, since the dust opacity at the Lyman limit frequency is as large as HI continuum for solar metallicity. Thus, it is reasonable that we have larger critical column density than obtained in Schaye & Dalla Vecchia (2008). On the other hand, in the present simulations, we assume  $Z = 10^{-2} Z_{\odot}$ . Therefore, the dust opacity at Lyman limit is smaller than HI continuum opacity by two orders of magnitude. As a result, dust opacity has much smaller impact on the self-shielding effects at such low metallicity. In any case, we would dare to mention that present results almost succeeded to probe the presence of star formation threshold column density proposed by Schaye (2004) utilizing the full 3D radiation hydrodynamics simulations. More realistic calculations for present-day galaxies including the effects of dust extinction are left for future works.

It is also worth noting that star formation rate (SFR) of the disk above the threshold column density is consistent with the observed value, although it is difficult to compare the present results directly with observed SFR, since we do not take into account the local stellar feedbacks, the effects of dust particles, metal enrichment followed by the radiative cooling by abundant metals. Despite of such issues, SFR could be obtained by the density PDF assuming the stars are formed in dense clumps within local free-fall time. It is given as

$$\dot{\Sigma}_* = \epsilon_c \sqrt{G \rho_c} \Sigma_{\text{disk}} f_c \quad (11)$$

where  $\epsilon_c$  is the star formation efficiency,  $\rho_c$  is the threshold density above which the gas is converted to stars,  $\Sigma_{\text{disk}}$  denotes the surface density of the disk, and  $f_c$  denotes the mass fraction of gas in the disk condensed into dense clumps with  $\rho > \rho_c$ .  $f_c$  is the quantity which can be obtained by integrating the density PDF above  $\rho_c$ . In the present set of simulations with radiative feedback, model Cr is the only one in which star formation is expected since self-shielded cold fragments emerges in the run. If we use  $\epsilon = 0.1$  and  $n_{\text{H, res}}$  to assess the threshold density  $\rho_c$ , we obtain  $f_c \simeq 0.066$ . Using the surface density of the disk in model Cr, the SFR is evaluated as  $\dot{\Sigma}_* = 0.03 M_{\odot} \text{ yr}^{-1} \text{ kpc}^{-2}$ . Although we cannot discuss the dependence of SFR on  $\Sigma_{\text{disk}}$ , the value is consistent with the observation (Kennicutt 1998). This reasonable agreement infer the validity of the present numerical models.

We also point out another standpoint on this issue by Susa & Umemura (2000a), in which they suggested that self-shielding from ultraviolet background

could be a key mechanism to determine the morphology of galaxies (Susa & Umemura 2000b), although their arguments based upon 1-dimensional radiation hydrodynamics calculations. Unfortunately, it is impossible to relate the present results to morphology bifurcation of galaxies, since we assume a disk by hand in our simulations performed so far. From this point of view, again we need to perform simulations from cosmological initial conditions.

## 6. CONCLUSION

In this paper, we perform radiation hydrodynamics simulations on the fragmentation of galactic disks under the ultraviolet radiation background. We find that ultraviolet radiation field strongly suppress the star formation in the disks in case the photoheating is not shielded enough. We emphasize that this suppression is different from photoevaporation effect, because the rotation velocities at the outer boundary of the disks in the present set of simulations are  $\sim 100$ km/s, which are fast enough to retain the

photoheated gas. In our simulations, we find a threshold column density of the disk ( $\sim 10^{21}$ cm $^{-2}$ ) above which the fragmentation is not suppressed. It is similar to the star formation threshold column density observed in nearby galaxies. Presence of such critical threshold would be one of the reason for the so-called down-sizing problem in nearby galaxies.

HS thanks the anonymous referee and K. Wada for helpful comments and discussions. HS also thanks M. Umemura, M. Ohta and H. Sato for their continuous encouragements. The analysis has been made with computational facilities at Center for Computational Science in University of Tsukuba, Konan University, and Rikkyo University. This work was supported in part by Inamori Research Foundation as well as Ministry of Education, Culture, Sports, Science, and Technology (MEXT), Grants-in-Aid, Specially Promoted Research 16002003.

## REFERENCES

Altay, G., Croft, R. A. C., & Pelupessy, I. 2008, ArXiv e-prints, 802, arXiv:0802.3698

Barkana, R., & Loeb, A. 1999, ApJ, 523, 54

Bate, M. R., & Burkert, A. 1997, MNRAS, 288, 1060

Boehringer, H., & Hensler, G. 1989, A&A, 215, 147

Babul, A., & Rees, M. J. 1992, MNRAS, 255, 346

Baldry, I. K., Balogh, M. L., Bower, R. G., Glazebrook, K., Nichol, R. C., Bamford, S. P., & Budavari, T. 2006, MNRAS, 373, 469

Corbelli, E., Galli, D., & Palla, F. 1997, ApJ, 487, L53

Cowie, L. L., Songaila, A., Hu, E. M., & Cohen, J. G. 1996, AJ, 112, 839

Dalgarno, A., & McCray, A. 1972, ARA&A, 10, 375

Draine, B. T., & Bertoldi, F. 1996, ApJ, 468, 269

Efstathiou, G. 1992, MNRAS, 256, 43P

Erb, D. K., Steidel, C. C., Shapley, A. E., Pettini, M., Reddy, N. A., & Adelberger, K. L. 2006, ApJ, 647, 128

Ferrara, A., & Tolstoy, E. 2000, MNRAS, 313, 291

Ferland, G. J. 2000, Revista Mexicana de Astronomia y Astrofisica Conference Series, 9, 153

Galli D. & Palla F. 1998, A&A, 335, 403

Gnedin, N. Y. 2000, ApJ, 542, 535

Gnedin, N. Y. & Abel, T., 2001, NewA, 6, 437

Iliev, I. T., et al. 2006, MNRAS371, 1057

Kauffmann, G., et al. 2003, MNRAS, 341, 54

Kennicutt, R. C., Jr. 1989, ApJ, 344, 685

Kennicutt, R. C., Jr. 1998, ApJ, 498, 541

Kitayama, T., Tajiri, Y., Umemura, M., Susa, H., & Ikeuchi, S. 2000, MNRAS, 315, L1

Kitayama, T., Susa, H., Umemura, M., & Ikeuchi, S. 2001, MNRAS, 326, 1353

Kodama, T., et al. 2004, MNRAS, 350, 1005

Martin, C. L., & Kennicutt, R. C., Jr. 2001, ApJ, 555, 301

Mellema, G., Iliev, I. T., Alvarez, M. A., & Shapiro, P. R. 2006, New Astronomy, 11, 374

Omukai, K. 2000, ApJ, 534, 809

Papovich, C., et al. 2006, ApJ, 640, 92

Qiu, J.-M., Feng, L.-L., Shu, C.-W., & Fang, L.-Z. 2007, New Astronomy, 12, 398

Reddy, N. A., Steidel, C. C., Fadda, D., Yan, L., Pettini, M., Shapley, A. E., Erb, D. K., & Adelberger, K. L. 2006, ApJ, 644, 792

Rijkhorst, E.-J., Plewa, T., Dubey, A., & Mellema, G. 2006, A&A, 452, 907

Robertson, B., & Kravtsov, A. 2007, ArXiv e-prints, 710, arXiv:0710.2102

Saitoh, T. R., Daisaka, H., Kokubo, E., Makino, J., Okamoto, T., Tomisaka, K., Wada, K., & Yoshida, N. 2008, ArXiv e-prints, 802, arXiv:0802.0961

Schaye, J. 2001, ApJ, 562, L95

Schaye, J. 2004, ApJ, 609, 667

Schaye, J., & Dalla Vecchia, C. 2008, MNRAS, 383, 1210

Shapiro, P.R., & Kang, H., 1987, ApJ, 318, 32

Spitzer, L. Jr. 1978, in Physical Processes in the Interstellar Medium (John Wiley & Sons, Inc. 1978)

Songaila, A. 2001, ApJ, 561, 153L

Steinmetz, M. & Müller, E. 1993, A&A, 268, 391

Susa, H., & Kitayama, T. 2000, MNRAS, 317, 175

Susa, H., & Umemura, M. 2000, ApJ, 537, 578

Susa, H., & Umemura, M. 2000, MNRAS, 316, L17

Susa, H., & Umemura, M. 2004, ApJ, 600, 1

Susa, H., & Umemura, M. 2004, ApJ, 610, 5L

Susa, H. 2006, PASJ, 455, 58

Susa, H., & Umemura, M. 2006, ApJ, 645, 93L

Susa, H. 2007, ApJ, 659, 908

Tasker, E. J., & Bryan, G. L. 2008, ApJ, 673, 810

Thacker, R.J., Tittley, E.R., Pearce, F.R., Couchman, H.M.P. & Thomas, P.A. 2000, MNRAS319, 619

Thoul, A. A. & Weinberg, D. H. 1996, ApJ, 465, 608

Toomre, A. 1964, ApJ, 139, 1217

Umemura, M. & Ikeuchi, S. 1984, Progress of Theoretical Physics, 72, 47

Umemura, M. 1993, ApJ, 406, 361

Wada, K., & Norman, C. A. 2007, ApJ, 660, 276

Whalen, D. J., & Norman, M. L. 2008, ApJ, 672, 287

Young, M. & Lo, Y. 1997, ApJ, 476, 127

Young, M. & Lo, Y. 1997, ApJ, 490, 710

Yoshida, N., Oh, S. P., Kitayama, T., & Hernquist, L. 2007, ApJ, 663, 687

TABLE 1  
COMMON PARAMETERS

symbol	numerical value employed	description
$N_{\text{nei}}$	50	Number of neighbor particles
$H_i$	100pc	Initial disk thickness
$R_{\text{disk}}$	3kpc	Initial disk radius
$T_i$	$10^4$ K	Initial disk temperature
$T_{\text{min}}$	300K	minimum temperature

TABLE 2  
MODEL DEPENDENT PARAMETERS

Label	$I_{21}$	$\rho_i [M_{\odot}/\text{pc}^{-3}]$	simulated time	# of SPH particles	$n_{\text{H, res}} [\text{cm}^{-3}]$	$\epsilon [\text{pc}]$
A	0	0.05	300 Myr	$1.28 \times 10^6$	235	3.05
B	0	0.1	120 Myr	$2.56 \times 10^6$	235	3.05
C	0	0.3	40 Myr	$7.68 \times 10^6$	235	3.05
Ar	1	0.05	350 Myr	$1.28 \times 10^6$	235	3.05
Br	1	0.1	200 Myr	$2.56 \times 10^6$	235	3.05
Cr	1	0.3	40 Myr	$7.68 \times 10^6$	235	3.05
B/2	0	0.1	120 Myr	$1.28 \times 10^6$	58.8	6.09
Br/2	1	0.1	120 Myr	$1.28 \times 10^6$	58.8	6.09
B/8	0	0.1	120 Myr	$3.20 \times 10^5$	3.67	24.4
Br/8	1	0.1	120 Myr	$3.20 \times 10^5$	3.67	24.4

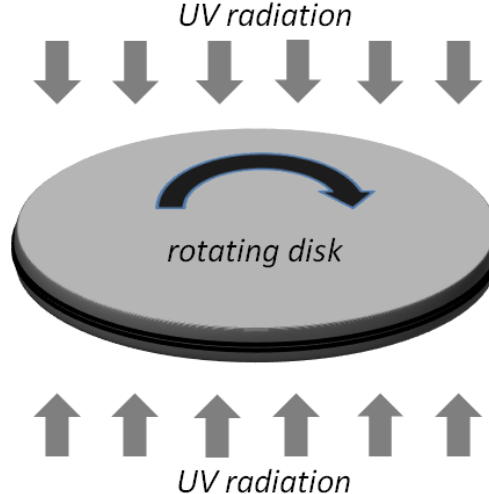


FIG. 1.— Schematic view of the assumed configuration. Rotating gas disk is embedded in a dark halo potential, which is irradiated by the ultraviolet background radiation. The light rays are assumed to be perpendicular to the disk.

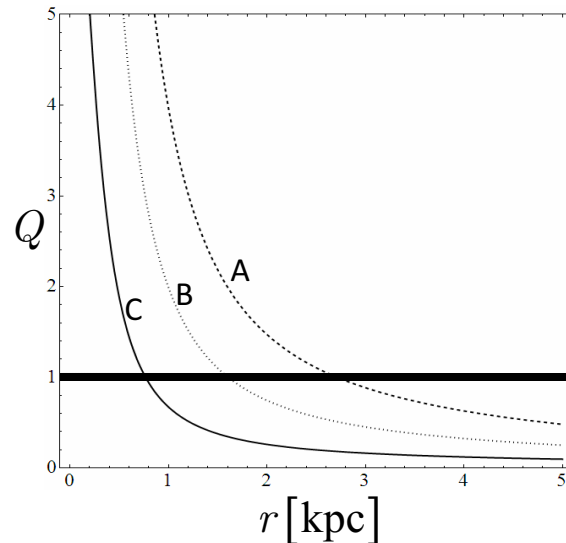


FIG. 2.—  $Q (= c_s \kappa / \pi G \Sigma)$  value is plotted as functions of radial coordinate in the disk. In case  $Q > 1$  is satisfied in a certain region of a disk, the region is gravitationally stable, otherwise not. Three curves correspond to the three models A, B and C assuming  $T = T_{\min}$ .

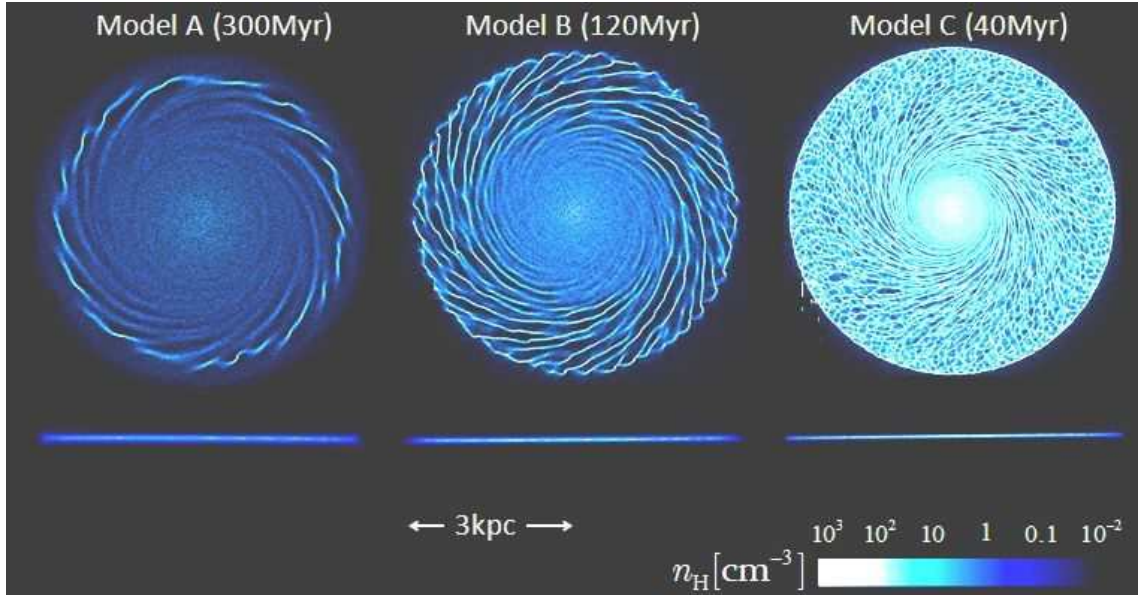


FIG. 3.— Face-on/edge-on view of the disks in three models A, B, and C are shown. These are the snapshots taken at  $t = 300$  Myr for model A,  $t = 120$  Myr for model B and  $t = 40$  Myr for model C, respectively. The color represents the density contrast, as shown in the legend.

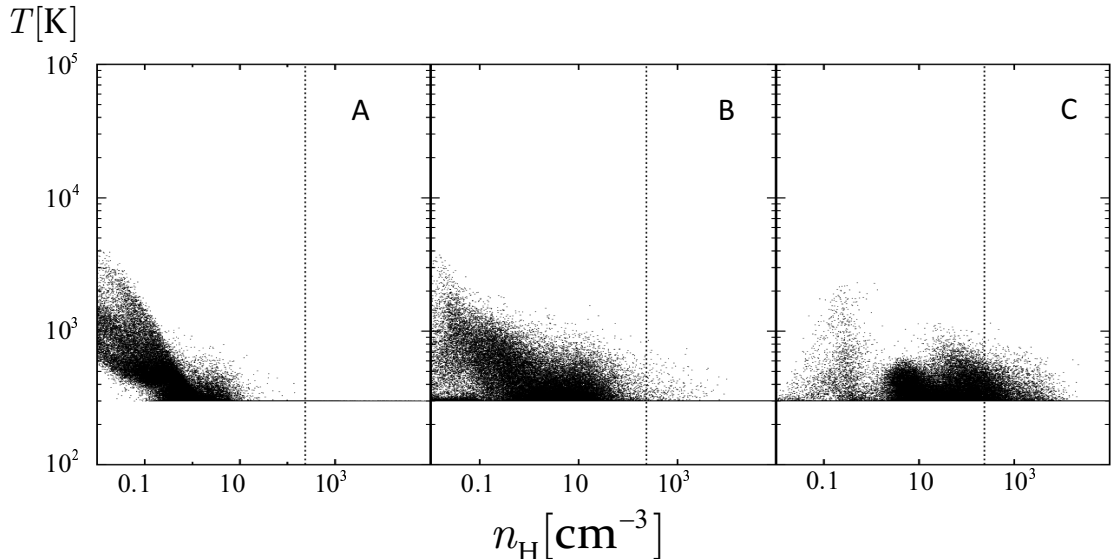


FIG. 4.— Phase diagram for models A, B, and C. Each dot represents each SPH particle. The vertical dotted lines represent  $n_{\text{H},\text{res}}$ .

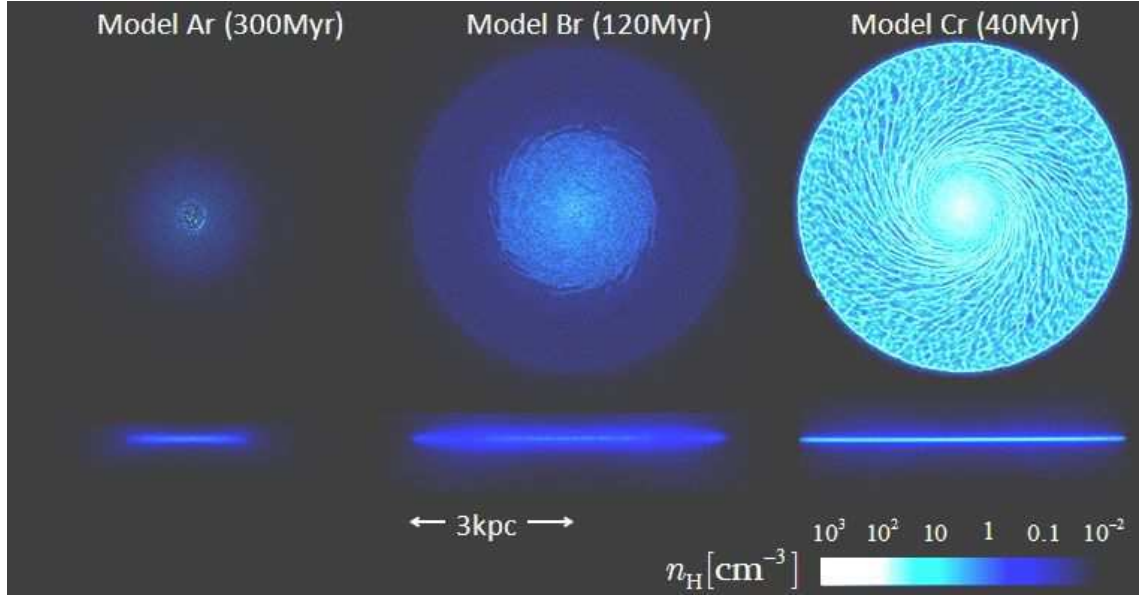


FIG. 5.— Same as Fig.3, except that the models are Ar, Br and Cr.

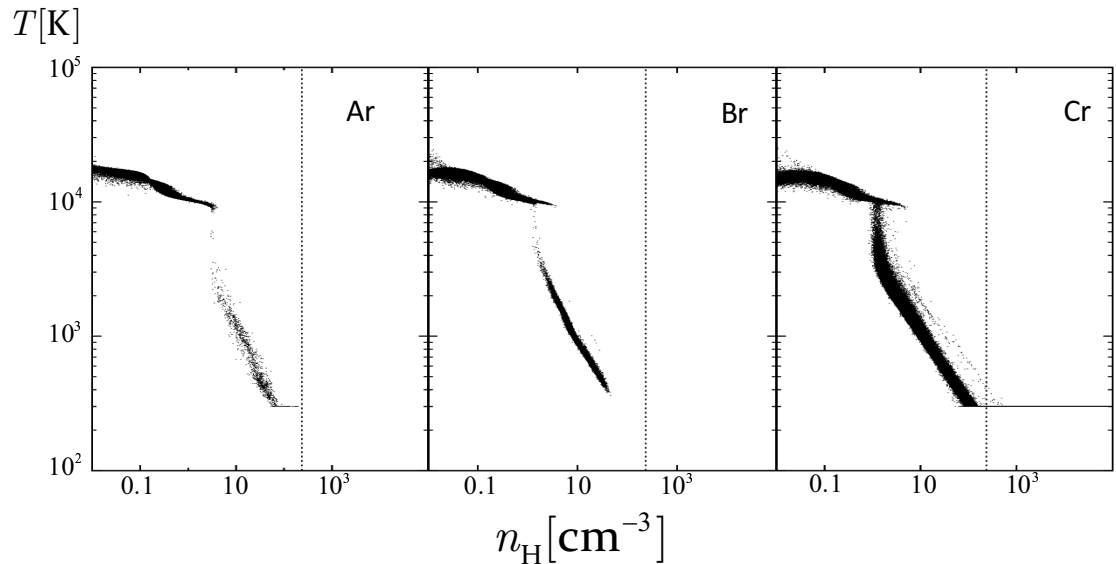


FIG. 6.— Same as Fig.4, except that models are Ar, Br and Cr.

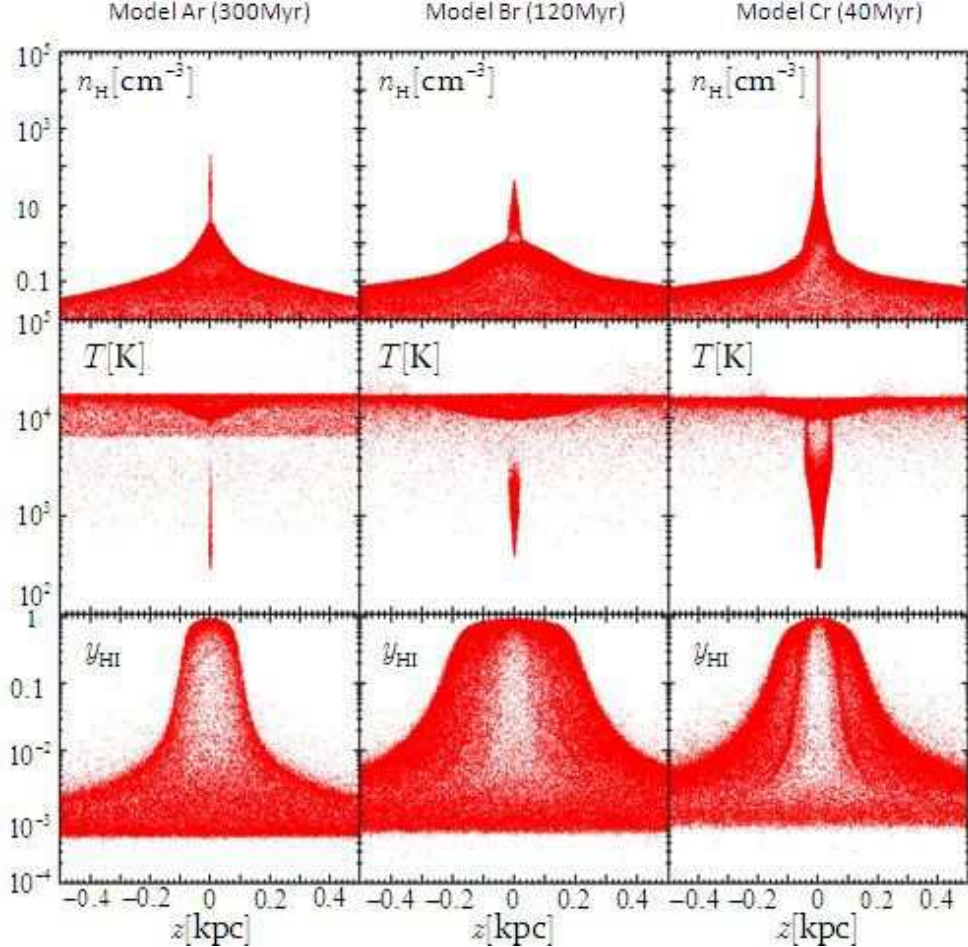


FIG. 7.— Various quantities in the disks are plotted as functions of vertical coordinate,  $z$ . The horizontal axes denote  $z$ , whereas vertical axes denote density (top), temperature (middle) and HI fraction  $y_{\text{HI}}$  (bottom). These are the snapshots taken at  $t = 300\text{Myr}$  for model A,  $t = 120\text{Myr}$  for model B and  $t = 40\text{Myr}$  for model C, respectively.

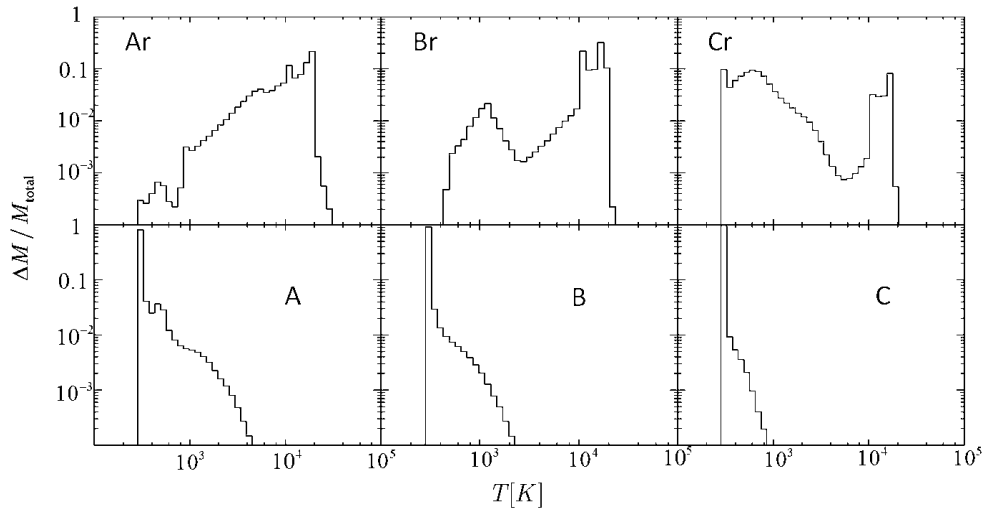


FIG. 8.— Temperature Probability Distribution Functions(PDFs) are shown for six models Ar,Br,Cr,A,B and C. Horizontal axes denote the temperature, whereas the vertical axes show the differential mass fraction  $\Delta M / M_{\text{total}}$  found within a logarithmic temperature bin  $\Delta(\log T) = 0.06$ . Here  $M_{\text{total}}$  is the total gas mass of the disk. The histograms denote temperature PDFs at  $t = 300\text{Myr}$  for models Ar and A,  $t = 120\text{Myr}$  for models Br and B,  $t = 40\text{Myr}$  for models Cr and C, respectively.

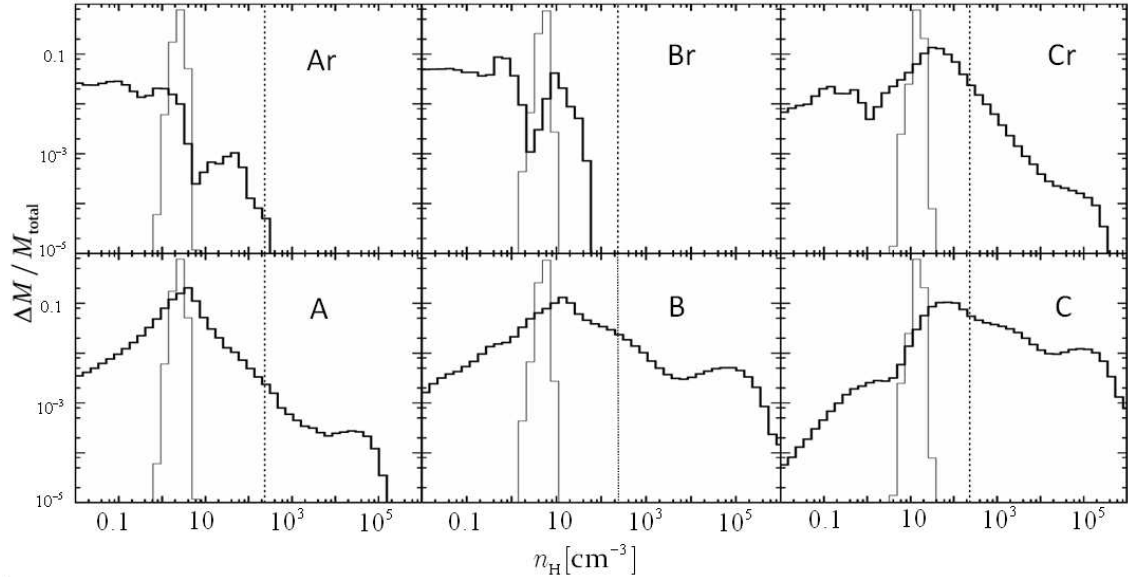


FIG. 9.— Density Probability distribution functions(PDFs) are shown for models A,B,C,Ar,Br and Cr. Horizontal axes denote the density, whereas the vertical axes show the differential mass fraction  $\Delta M / M_{\text{total}}$  found within a logarithmic density bin  $\Delta(\log n_{\text{H}}) = 0.18$ . The histogram drawn by thin solid lines denote the initial PDFs in the models. The thick solid lines denote the evolved PDFs at  $t = 300\text{Myr}$  for models A and Ar,  $t = 120\text{Myr}$  for models B and Br,  $t = 40\text{Myr}$  for models C and Cr, respectively. The vertical dotted thin lines show the resolution limits of the runs.

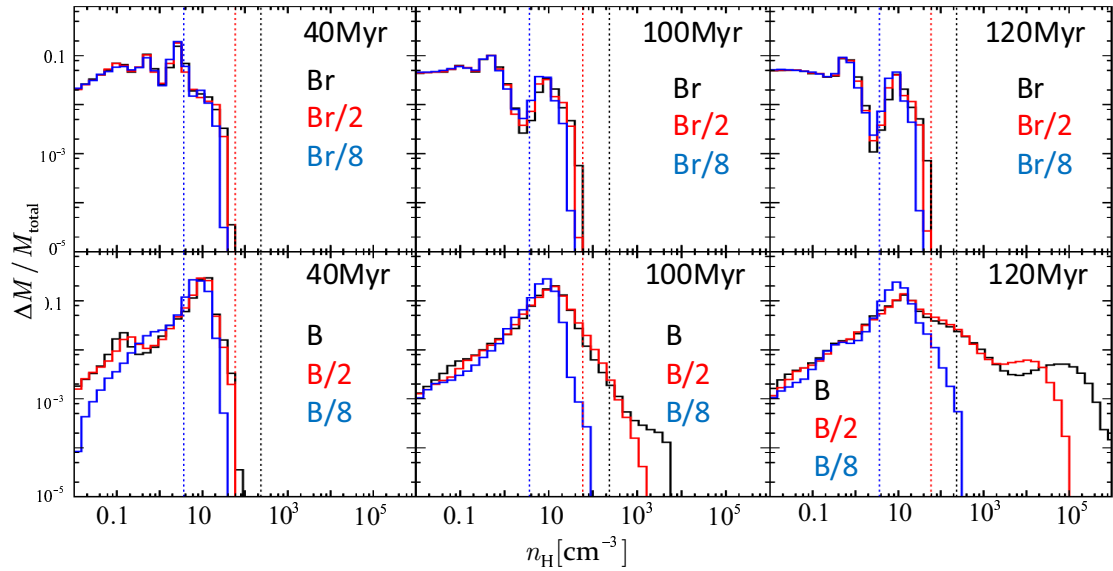


FIG. 10.— PDFs in models B and Br are compared to the results from the low resolution runs(B/2,Br/2,B/8,Br/8). The axes are the same as Fig.9. Top three panels :the PDFs for models Br(black histogram) , Br/2(red), Br/8(blue) at  $t = 40\text{Myr}$ (left),  $100\text{Myr}$ (middle) and  $120\text{Myr}$ (right).Density resolution limits,  $n_{\text{H},\text{res}}$ , corresponding to the runs Br, Br/2 and Br/8 are shown as the vertical dotted lines with colors same as the histograms. Bottom panels : PDFs for models B, B/2 and B/8 at three epochs. The colors are same as the top panels.